Photoinduced electron transfer in non-covalent complexes of C_{60} and phosphangulene oxide derivatives

A. J. Stasyuk,*[a,b] O. A. Stasyuk,[a] M. Solà*[a] and A. A. Voityuk*[a,c]

a. Institut de Química Computacional and Departament de Química, Universitat de Girona, C/ Maria Aurèlia Capmany 69, 17003 Girona, Spain

b. Faculty of Chemistry, University of Warsaw, Pasteura 1, 02-093 Warsaw, Poland

c. Institució Catalana de Recerca i Estudis Avancats (ICREA), 08010 Barcelona, Spain

Abstract: Investigation of photoinduced electron transfer (PET) in a series of experimentally reported complexes of fullerene with phosphangulene oxides shows that the replacement of O atoms in the bridge of phosphangulene with S atoms promotes efficient and ultrafast ET from fullerene to phosphangulene oxide in **PGO^{OSS}⊃C$_{60}$** and **PGO^{SSS}⊃C$_{60}$** complexes. The results obtained can be useful in development of photovoltaic devices based on phosphangulenes.

Introduction

Phosphangulenes are tertiary phosphines with a hexacyclic structure and a distinctive conical shape. The hexacyclic structure is the same as that of triangulene by replacing the central C atom by a phosphorus atom and the three CH bridged groups by O atoms. In 1997, Krebs and co-workers reported a unique triarylphosphine molecule bridged by three oxygen atoms and called its "phosphangulene".[1,2] The synthesis of singlet ground state phosphangulenes preceded that of triangulene in its triplet ground state that took place 10 years after.[3] Analysis of crystallographic data revealed that the molecule of phosphangulene has C_{3v} symmetry. Its dipole moment was found to be 3.3 ± 0.2 D.[1] In crystalline form, the molecules of phosphangulene stack on top of each other (like a traffic cones) providing the trigonal space group R3m.[4] Converting phosphangulene to corresponding phosphine oxide slightly increases a cone angle but retains molecular symmetry. However, new molecular shape prevents efficient molecular stacking. Having lost main factors for direct crystallization (topology and aromatic $\pi-\pi$ interactions), phosphangulene oxide molecules form offset clamshell pairs held together by multiple C−H···π interactions, and tend to form multiple polymorphs.[5] The inability of phosphangulene oxide to crystallize optimally predisposes them to form structures with other molecules. In 2014, Yamamura, Nabeshima, and co-workers reported a successful usage of chiral phosphangulene oxide for recognition of fullerenes.[6, 7] They also studied in detail how cone values in phosphangulenes and phosphangulene chalcogenides affect their ability to encapsulate C_{60} as a guest molecule in co-crystals. It was clearly demonstrated that the bowl-shape geometry gives control over the assembly architectures and results in the formation of chiral capsules or achiral pseudo-cage.[8] The effect of the bridge atom on the cone angle, bowl-shape geometry and packing structures of phosphangulenes was systematically studied by replacing oxygen bridge atoms by sulfur. It has been demonstrated that the depth of bowl becomes shallower as the number of bridging sulfur atoms increases.[9,10] Later D. Wuest and co-workers significantly expanded the understanding of the role of chalcogenides in the formation of co-crystals with fullerenes.[11-13] Their

structural studies showed that phosphangulene chalcogenides disrupt the normal organization of fullerenes, increasing the degree of their separation but not eliminating fullerene−fullerene contacts necessary for direct electronic communication.[14,15]

Here we report the electronic properties of four complexes of C_{60} with phosphangulene oxide and its derivatives. Using time-dependent density functional theory (TDDFT), we investigate the ability of these complexes to efficient photoinduced electron transfer (PET).

Results and discussion

Ground state properties

The π–π and CH···π interactions between PG units significantly complicate co-crystallization of phosphangulenes (PG) with fullerenes. Thus, co-crystals of PGs with C_{60} or C_{70} fullerenes have not been reported, despite efforts to obtain them. In contrast, phosphangulene oxides (PGO), due their unfavorable shape, form the staggered clamshell pairs, which are only held together by several CH···π interactions. To quantify the interaction strengths in PG dimer and PG and PGO complexes with C_{60} we computed the interaction energies (ΔE_{int}) and performed their decomposition analysis using the Morokuma[16] scheme (Table S1 and Figure S1 in SI). For the complexes **PG^{OOO}⊃PG^{OOO}, PG^{OOO}⊃C_{60}**, and **PGO^{OOO}⊃C_{60}**, ΔE_{int} was found to be -19.36, -17.54 and -18,3 kcal/mol, respectively. Thus, PG dimer has a stronger interaction energy compared to the complex of PG with C_{60}, mainly due to the stronger dispersion interactions. Similarly, the dispersion term is responsible for a stronger interaction energy in **PGO^{OOO}⊃C_{60}** compared to **PG^{OOO}⊃C_{60}**.

The distinctive feature of the electron-rich aromatic surface of phosphangulene chalcogenides, which geometrically and electronically complements the electron-poor π-surface of fullerene, prompts us to study in detail the photoinduced electron transfer properties in four **PGO^{OOO}⊃C_{60}**, **PGO^{OOS}⊃C_{60}**, **PGO^{OSS}⊃C_{60}**, and **PGO^{SSS}⊃C_{60}** binary van der Waals (vdW) complexes of phosphangulene oxide and its derivatives with **C_{60}** (Figure 2). The equilibrium geometries of the systems were optimized using B3LYP-D3(BJ)/Def2-SVP.

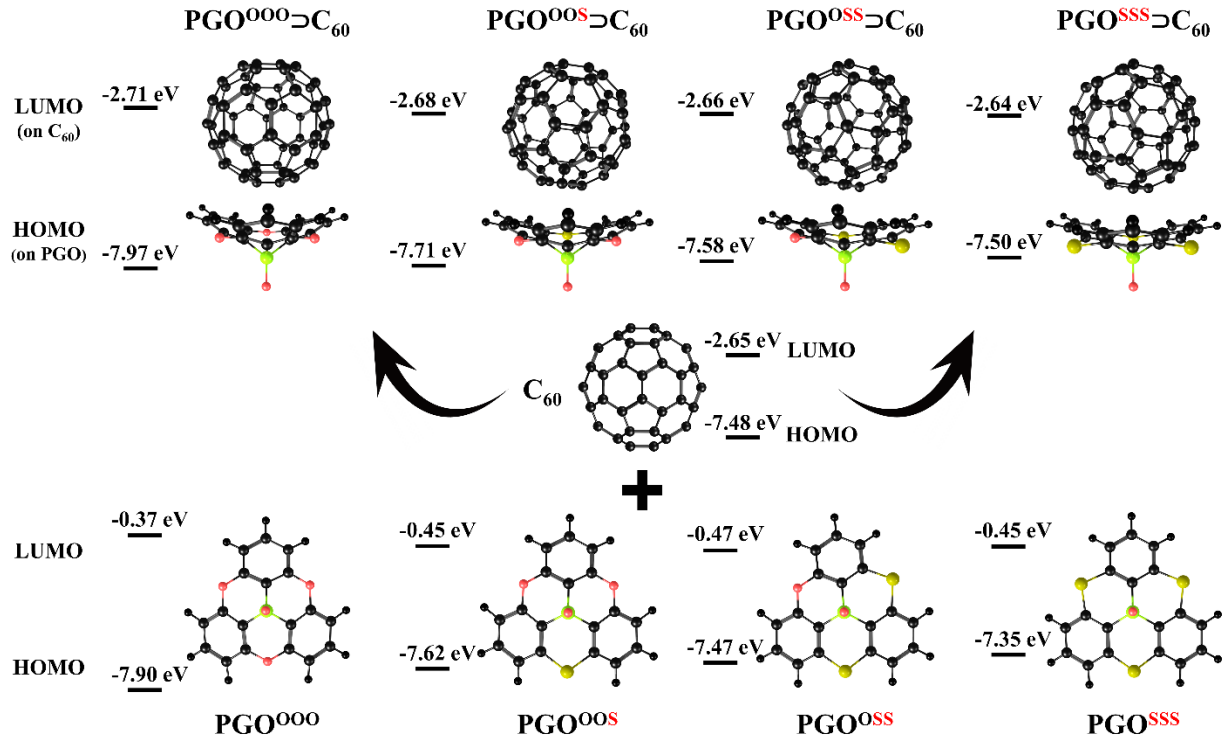

Figure 1. Structure and HOMO and LUMO energies of the studied complexes.

As seen in Figure 1, the formation of complexes has a rather weak effect on the HOMO and LUMO energies of the fragments. The LUMO energy of **C_{60}** changes within 0.1 eV whereas the decrease in the HOMO energies of PGOs does not exceed 0.15 eV. The small differences in the HOMO and LUMO energies in complexes and individual fragments indicate the absence of charge separation in the ground state of the complexes. Indeed, the population analysis for the systems does not reveal any significant charge transfer between the host and guest molecules (Table S2, SI).

To assess the stability of complexes, the interaction energy (ΔE_{int}) between **PGOs** and **C_{60}** was computed at the B3LYP-D3(BJ)/TZ2P level of theory. For **PGO^{OOO}⊃C$_{60}$**, **PGO^{OOS}⊃C$_{60}$**, **PGO^{OSS}⊃C$_{60}$**, and **PGO^{SSS}⊃C$_{60}$** systems, ΔE_{int} was found to be -18.3, -18.9, -20.2, and -20.6 kcal/mol, correspondingly. According to the energy decomposition analysis all complexes characterized by a similar nature of non-covalent interactions (Table S3, SI). Among the binding forces (electrostatic, orbital and dispersion interactions), the dispersion term dominates with a contribution of 54 to 57%; it is followed by the electrostatic term (with a contribution of about 30%) and the orbital interactions, which give no more than 15%. The subsequent replacement of the oxygen atom by sulfur in the bridge when passing from **PGO^{OOO}⊃C$_{60}$** to **PGO^{SSS}⊃C$_{60}$** leads to a slight increase in the interaction energy. The topological analyses performed using the Bader's Atoms in Molecules theory (QTAIM) and the reduced density gradient non-covalent index (RDG NCI) did not reveal significant differences between the complexes (Figures S2-S4, Table S4).

Singlet excited states

Simulations of excited states were performed using the TD-DFT method with the CAM-B3LYP-D3(BJ)/def2-SVP scheme.[17,18] The guest (**C_{60}**) and host (**PGO**) molecule contributions to the excited state electronic density were analyzed for the lowest 100 excited states of each complex. Three types of excited states

have been identified: (1) locally excited (LE) states, where excitation is mostly localized on one fragment with a charge separation value CS < 0.1 ***e***. There are two types of LE excitations: LE_1 that occurs on **C_{60}**, and LE_2 that occurs on the host molecule; (2) charge transfer (CT) states with electron density transferred between the fragments (CS > 0.8 ***e***), and (3) mixed states with a significant contribution of both LE and CT (0.1***e*** < CS < 0.8***e***).

Table 1. Singlet excitation energies (E_x, eV), main singly excited configuration (HOMO(H)–LUMO(L)) and its weight (W), oscillator strength (f), and extent of charge separation (CS, e) or exciton localization (X) for **$PGO^{OOO}\supset C_{60}$**, **$PGO^{OOS}\supset C_{60}$**, **$PGO^{OSS}\supset C_{60}$**, and **$PGO^{SSS}\supset C_{60}$** complexes.

	Supramolecular host-guest systems			
	$PGO^{OOO}\supset C_{60}$	**$PGO^{OOS}\supset C_{60}$**	**$PGO^{OSS}\supset C_{60}$**	**$PGO^{SSS}\supset C_{60}$**
	LE_1 (Fullerene C_{60})			
Ex	2.562	2.551	2.559	2.561
Transition (W)	H – L+2 (0.29)	H – L+1 (0.48)	H – L (0.37)	H-1 – L (0.28)
f	<0.001	<0.001	<0.001	<0.001
X	0.957	0.968	0.971	0.972
	LE_2 (Host PGO)[a]			
Ex	4.818	4.580	4.572	4.344
Transition (W)	H-5 – L+6 (0.26)	H-5 – L+6 (0.29)	H-6 – L+7 (0.29)	H-5 – L+6 (0.10)
f	0.069	0.029	0.070	<0.001
X	0.675	0.789	0.721	0.448
	Most absorptive transition			
Ex	4.403	4.382	4.372	4.384
Transition (W)	H-4 – L+3 (0.17)	H-2 – L+5 (0.17)	H – L+4 (0.28)	H-4 – L+4 (0.14)
f	0.395	0.386	0.374	0.368
Localization	**C_{60}**	**C_{60}**	**C_{60}**	**C_{60}**
X	0.973	0.956	0.910	0.884
	CT (Host PGO → Fullerene C_{60})			
Ex	4.853	3.448	3.398	3.351
Transition (W)	H-8 – L (0.48)	H-5 – L+1 (0.59)	H-5 – L+1 (0.66)	H-5 – L (0.37)
f	0.010	0.006	0.002	0.008
CS	0.880	0.804	0.891	0.932

[a] In all complexes the LE_2 state is partially delocalized over C_{60} unit.

In the gas phase, the 100 lowest vertical singlet excitation energies of the complexes are found in the range from 2.55 to 5.30 eV. The LE_1 state with the excitation on **C_{60}** was found to be the lowest excited state. The LE_2 states with the exciton localized on **PGOs** lie by 2.2-1.8 eV higher in energy, depending on phosphangulene type. The highly absorptive states, with oscillator strength around 0.35-0.40, were found for each complex at ca. 4.4 eV (Table 1).Among the studied excited states, only one type of CT state was found, which corresponds to the electron transfer from **PGOs** to **C_{60}** leading to **$PGO^{+}\supset C_{60}^{-}$** (Table 1). The CT state in **$PGO^{OOO}\supset C_{60}$** lies at 4.85 eV and thus is significantly higher in energy than both LE states. Replacing at least one oxygen atom by sulfur in phosphangulene oxide increases the HOMO energy (Figure 1) strongly affecting the energetics of CT states. In **$PGO^{OOS}\supset C_{60}$**, **$PGO^{OSS}\supset C_{60}$**, and **$PGO^{SSS}\supset C_{60}$** systems, the CT states are found at 3.45, 3.40 and 3.35 eV, respectively.

The Rehm-Weller analysis is widely used in photophysical studies to estimate the free energy for ET reactions in donor acceptor systems using experimental data for the individual D and A . Let us compare the TD-DFT results for the **PGO^{SSS}⊃C$_{60}$** complex with estimates derived using the Rehm-Weller equation[19] $\Delta G_{ET} = E_D^{ox} - E_A^{red} - \Delta E_{Coulombic} - E_{S/T}^*$. Unfortunately, experimental values of the oxidation potential for phosphangulenes still seem to be unknown. Thus, we use the computed values of E_A^{red} and E_D^{ox} . An estimate of ΔG_{ET} (0.51 eV) obtained with the Rehm-Weller equation is in good agreement with the value of 0.79 eV calculated by TD DFT (see Table S5, SI). The observed deviation is mainly due to approximate estimation of $\Delta E_{Coulombic}$: the effective distance between the centers of charge in D and A may differ from the center-to-center distance we used.

Additionally, we analyzed the excited states in terms of natural transition orbitals (NTOs). The NTOs representing the LE and CT states in the complexes are shown in Figures S5-S8 in SI.

Effects of environment

A well-proven COSMO-like model[20-22] with dichloromethane (DCM) as the solvent was applied to estimate the effect of polar environment on electronic excitations. The ground state (GS) solvation energies of **PGO^{OOO}⊃C$_{60}$**, **PGO^{OOS}⊃C$_{60}$**, **PGO^{OSS}⊃C$_{60}$**, and **PGO^{SSS}⊃C$_{60}$** are computed to be -0.18, -0.16, -0.14, and -0.14 eV, respectively. The observed slight decrease in GS solvation energies correlates with the decrease in the dipole moment of the complexes from 5.16 to 4.00 D when moving from **PGO^{OOO}⊃C$_{60}$** to **PGO^{SSS}⊃C$_{60}$**. The difference of the dipole moments between LE and GS states is small and varies from 0.66 to 3.88 D. Because of that, the solvation energies of GS, LE_1, and LE_2 states are similar (Table S6).

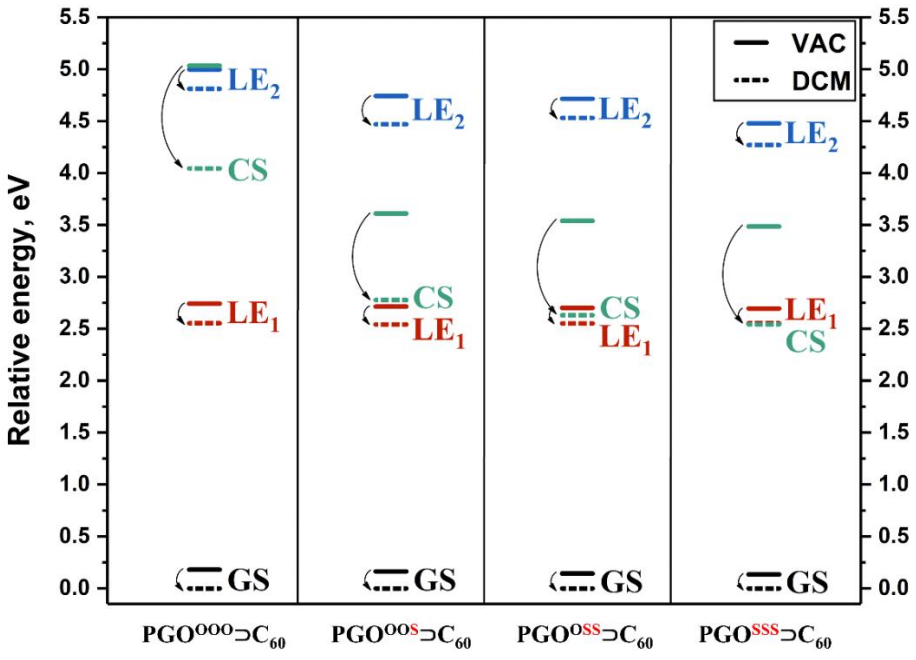

Figure 2. Relative energies (in eV) of GS, LE_1, LE_2, and CT states of the **PGO^{OOO}⊃C$_{60}$**, **PGO^{OOS}⊃C$_{60}$**, **PGO^{OSS}⊃C$_{60}$**, and **PGO^{SSS}⊃C$_{60}$** complexes computed in vacuum (VAC) and dichloromethane (DCM).

As expected, in contrast to LE transitions, CT excitations lead to a significantly greater increase in the dipole moment of the complexes. The change in dipole moment ($\Delta\mu^{CT}$) computed for **PGO^{OOO}⊃C$_{60}$**, **PGO^{OOS}⊃C$_{60}$**, **PGO^{OSS}⊃C$_{60}$**, and **PGO^{SSS}⊃C$_{60}$**, is 23.9, 20.2, 22.7, and 23.9 D, respectively. The solvation

energies of the CT states are equal to -0.99, -0.83, -0.91, and -0.94 eV, correspondingly. The $\Delta\mu^{CT}$ and solvation energies for the states of interest are listed in Table S6. Figure 2 shows the solvent effects on the LE and CT excitations. The relative stabilization of the CT state of **PGO^{OOO}⊃C$_{60}$** and **PGO^{OOS}⊃C$_{60}$** in DCM is insufficient to reorder the CT and LE states. However, the energy gap between the LE_1 and CT states becomes almost negligible by solvation of **PGO^{OSS}⊃C$_{60}$** and **PGO^{SSS}⊃C$_{60}$**.

Charge transfer complexes and electron transfer rates

The electron-donating properties of phosphangulene and its chalcogenide derivatives as well as their ability to build non-covalent complexes with fullerenes make them promising candidates for photovoltaic applications. Apart of the PGO system, we also studied the PET processes occurring in several structurally similar non-covalent complexes of **C$_{60}$** with molecules widely used in photovoltaics: tribenzosubporphine (**TBSubP**), corannulene (**Cora**) and sumanene (**Suma**). The host concave molecules and the general structure of the non-covalent complexes are shown in Figure 3.

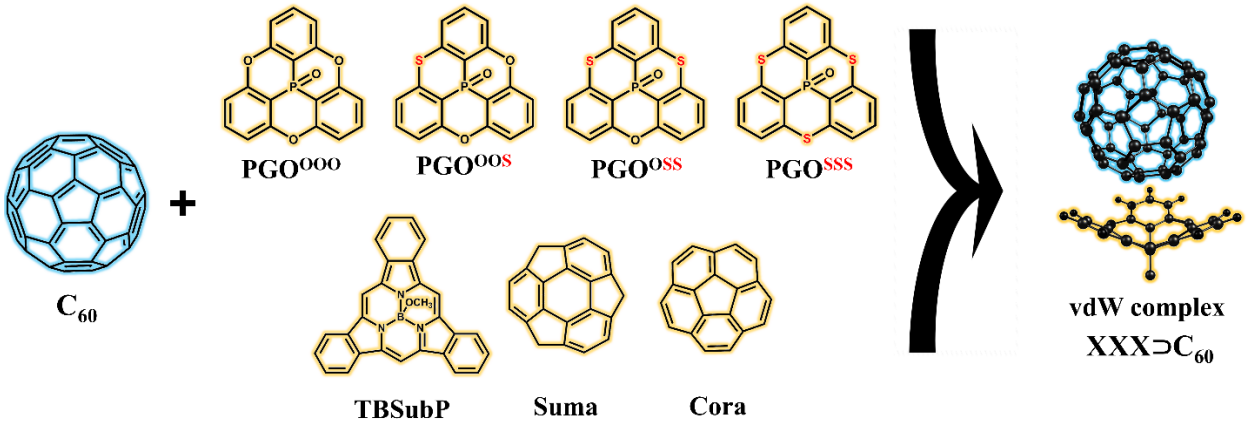

Figure 3. Structure of selected host molecules (XXX) and their Van-der-Waals complexes **XXX⊃C$_{60}$** with C_{60}.

A direct population of the CT states by the light absorption is unlikely because of the low oscillator strength ($f < 0.01$). However, they can be generated by the decay of most absorbing (MA) excited states, or low-lying LE states. To find out which mechanism is preferable depending on the polarity of the environment, we studied two cases - **PGO^{OOO}⊃C$_{60}$** and **PGO^{SSS}⊃C$_{60}$** (Figure 4).

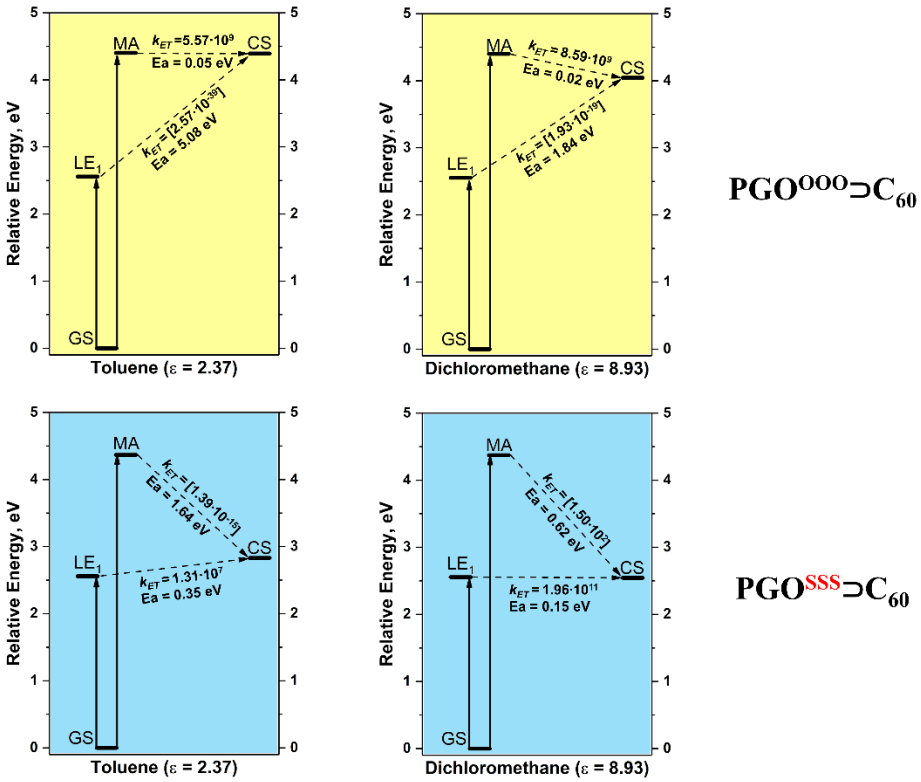

Figure 4. Computed rates of photoinduced electron transfer in **PGO^{OOO}⊃C$_{60}$** (top) and **PGO^{SSS}⊃C$_{60}$** (bottom) in toluene and dichloromethane.

For **PGO^{OOO}⊃C$_{60}$**, the generation of the CS state by the decay of LE_1 cannot take a place due to the big positive Gibbs energy (Table S7, SI). In contrast, the generation of the CS from the strongly absorbing excited state is a thermodynamically favorable process. The computed rates are found to be $5.57 \cdot 10^9$ and $8.59 \cdot 10^9$ sec^{-1} in toluene and DCM solvents, respectively (Table S7, SI). For the **PGO^{SSS}⊃C$_{60}$** complex, the generation of the CS state from the strongly absorbing excited state occurs very slowly in the inverted Marcus regime ($-\Delta G^0 > \lambda$). On the other hand, the generation of the CS state from LE1 takes place in both solvents while in toluene this reaction is significantly slower than in DCM ($1.31 \cdot 10^7$ vs $1.96 \cdot 10^{11}$ sec^{-1}). Thus in **PGO^{OOO}⊃C$_{60}$**, the CS state can be generated only by the decay of the highly absorbing excited state. For other complexes, however, this deactivation channel is unfeasible and the charge separation occurs from the LE_1 state. The dependence of the electron transfer rate for LE1→CT reaction on Gibbs free energy for **PGO^{SSS}⊃C$_{60}$** complex in DCM is provided in Figure S9, SI.

Geometry optimization of the vdW complexes shown on Figure 3 and calculation of their excited states were performed using the same methods as described in previous sections. The properties of the LE and CT states in the gas-phase and DCM are given in Table S8. The rates of electron transfer k_{ET} were calculated using the semi-classical method by Ulstrup and Jortner.[23,24] Within this approach, the intramolecular relaxation associated with ET is described by an effective vibrational mode, and the rate is controlled by four parameters: electronic coupling V_{ij} of the initial and final states, solvation reorganization energy λ_s, reaction Gibbs energy ΔG^0, and effective Huang-Rhys factor S_{eff}. The computed parameters, as well as the ET rates in DCM solvent are listed in Table 2. The k_{ET} values were obtained using the effective frequency

of 1600 cm^{-1}, which corresponds to the stretching of C=C bonds. Note that the calculated ET rates do not change significantly by changing the effective frequency from 1400 to 1800 cm^{-1} (Table S9, SI).

Table 2. Ground and excited state properties, and electron transfer parameters computed for the complexes **XXX⊃C$_{60}$**: interaction energy (ΔE_{int}, kcal/mol), HOMO energy of host fragment **XXX** (HOMO, eV), excitation energy (E, eV), exciton localization (X) on **C$_{60}$** fragment, extent of charge transfer (CT, e), Gibbs energy (ΔG^0, eV), electronic coupling ($|V_{ij}|$, eV), activation barrier (Ea, eV), internal and solvent reorganization energies (λ_i and λ_s, eV), and electron transfer rate (k_{ET}, s^{-1}).

	XXX⊃C$_{60}$	ΔE_{int}	HOMO of **XXX**	LE_1[a]	CT from **XXX** to **C$_{60}$**	ΔG^0 [b]	ΔEa[c]	$\|V_{ij}\|$	Reorg. Energy		k_{ET}
									λ_i[d]	λ_s	
1	**PGO^{OOO}**	-18.3	-7.97	E=2.55 X=0.96	E=4.05 CT=0.88	1.49	1.84	$1.16\cdot10^{-2}$	0.188	0.403	n/a[e]
2	**PGO^{OOS}**	-18.9	-7.71	E=2.54 X=0.97	E=2.78 CT=0.80	0.24	0.28	$1.68\cdot10^{-2}$	0.208	0.312	$7.27\cdot10^{8}$
3	**PGO^{OSS}**	-20.2	-7.58	E=2.55 X=0.97	E=2.63 CT=0.89	0.08	0.18	$1.41\cdot10^{-2}$	0.196	0.356	$3.41\cdot10^{10}$
4	**PGO^{SSS}**	-20.6	-7.50	E=2.55 X=0.97	E=2.54 CT=0.93	-0.01	0.14	$1.61\cdot10^{-2}$	0.214	0.389	$1.96\cdot10^{11}$
5	**TBSubP**	-23.5	-6.13	E=2.54 X=0.97	E=1.60 CT=0.98	-0.94	0.11	$1.75\cdot10^{-2}$	0.154	0.333	$7.05\cdot10^{10}$
6	**Suma**	-17.4	-7.04	E=2.55 X=0.93	E=2.52 CT=0.87	-0.03	0.13	$3.97\cdot10^{-3}$	0.166	0.410	$5.30\cdot10^{9}$
7	**Cora**	-16.8	-7.73	E=2.55 X=0.97	E=3.16 CT=0.86	0.61	0.61	$9.35\cdot10^{-3}$	0.170	0.413	$5.69\cdot10^{3}$

[a] The lowest LE states are localized on **C$_{60}$**; [b] Gibbs energy of electron transfer $LE_1 \rightarrow CT$; [c] An activation barrier for $LE_1 \rightarrow CT$ reaction [d] An effective value of the Huang-Rhys factor $S_{eff} = \lambda_i/\hbar w_{eff}$, where $\hbar w_{eff}$ is set to 1600 cm^{-1}. [e] ET does not occur due to highly positive Gibbs energy.

The complexes of phosphangulene oxide with fullerene are characterized by a rather small internal reorganization energies, which ranges from 0.19 to 0.21 eV. Because of its highly positive Gibbs energy, the $LE_1 \rightarrow CS$ charge separation process in **PGO^{OOO}⊃C$_{60}$** is unlikely (the estimated rate constant is extremely small and cannot be reliably determined). Rather high activation barrier is responsible for slow electron transfer in **Cora⊃C$_{60}$**. For **PGO^{OSS}⊃C$_{60}$** and **PGO^{SSS}⊃C$_{60}$** complexes, the PET occurs in normal Marcus regime ($|\Delta G^0| < \lambda$) on a picosecond time scale (τ is 29 and 5 ps, respectively). The estimated rate constants corroborate unambiguously the ultrafast charge separation between **C$_{60}$** and phosphangulene oxide in **PGO^{OSS}⊃C$_{60}$** and **PGO^{SSS}⊃C$_{60}$**. The PET in these complexes is just as efficient as in the complex of subporphyrin with fullerene, which is known for its unique electron transfer properties.[25] Note that in **TBSubP⊃C$_{60}$**, the excitation takes place with high oscillator strength occurs on both units and the CS can be generated by the decay of both LE states. The computed rates of these processes are comparable. The characteristic time for the charge separation from the LE states localized on **C$_{60}$** and **TBSubP** is found to be 0.14 and 0.72 ns, respectively (for details see Table S10, SI). Thus, the PET in **TBSubP⊃C$_{60}$** complex occurs on the sub-nanosecond time scale, regardless of the exciton position. The PET in the complex with polycyclic aromatic hydrocarbon **Suma⊃C$_{60}$** is one to two orders of magnitude slower than in **PGO^{OSS}⊃C$_{60}$** and **PGO^{SSS}⊃C$_{60}$**. A very slow PET found In **Cora⊃C$_{60}$** is due to a low-lying HOMO and high symmetry of **Cora,** which prevents an efficient solvation of CT states.

Usually, the effect of internal geometry reorganization on ΔG is rather small for large conjugated systems.[20,26] To get more insight, we studied the effect of geometry relaxation on the rate of charge separation in **PGO^{SSS}⊃C$_{60}$** in DCM. The found effect is small. The ΔG^0 for the ET process in PGO^{SSS} complex changes insignificantly, from -0.01 eV to -0.06 eV. This in turn increases the ET rate by a factor of 2, from $1.96 \cdot 10^{11}$ to $4.31 \cdot 10^{11}$ (Table S11, SI).

Conclusions

In conclusion, the photoinduced charge separation in **PGO^{OOO}⊃C$_{60}$**, **PGO^{OOS}⊃C$_{60}$**, **PGO^{OSS}⊃C$_{60}$**, and **PGO^{SSS}⊃C$_{60}$** complexes has been studied in detail using the TD-DFT approach. Replacing O atoms with less electronegative S atoms promotes the HOMO energy increase and facilitates electron transfer from phosphangulene oxide to **C$_{60}$** unit. The **PGO^{OSS}⊃C$_{60}$** and **PGO^{SSS}⊃C$_{60}$** reveal the ultrafast photoinduced electron transfer on the picosecond time scale. The PET in which CS state generated by the decay of lowest-lying LE state in **PGO^{OOO}⊃C$_{60}$** and **PGO^{OOS}⊃C$_{60}$** is hindered by the positive Gibbs energy. Thus, a unique set of features inherent in phosphangulenes can be enriched with their ability to efficiently transfer electrons in complexes with fullerene.

Experimental

Quantum-chemical calculations

Geometry optimization of the complexes was performed at the B3LYP/def2-SVP level of theory in the ORCA 4.2.1 program.[27,28] The host-guest interaction energy was computed at the B3LYP/def2-TZVP level. Vertical excitation energies were calculated using TD-DFT method[29] with CAM-B3LYP/def2-SVP. In all cases, the empirical dispersion D3 correction with Becke–Johnson damping,[30,31] was employed. The population analysis within Mulliken, Löwdin, Hirshfeld, and CM5 schemes was carried out using Gaussian 16 (Rev. A03).[32] Topological analysis of the electron density distributions was conducted using the QTAIM[33,34] and NCI technique.[35,36] To visualize molecular structures, NCI isosurfaces, and natural transition orbitals, Chemcraft 1.8. program[37] was used.

Analysis of excited states

The quantitative analysis of exciton delocalization and charge transfer in the donor-acceptor complexes was carried out in terms of transition density.[38-40] The analysis was performed in the Löwdin orthogonalized basis for convenience. The matrix $^{\lambda}\mathbf{C}$ of orthogonalized molecular orbital (MO) coefficients was obtained from the coefficients **C** in the original basis $^{\lambda}\mathbf{C} = \mathbf{S}^{1/2}\,\mathbf{C}$, where **S** is the atomic orbital overlap matrix. The transition density matrix T^{0i} for an excited state Φ^* constructed as a superposition of singly excited configurations (where an occupied MO ψ_i is replaced a virtual MO ψ_a) is computed as:

$$T^{0i}_{\alpha\beta} = \sum_{ia} A_{i\to a}\, {}^{\lambda}C_{\alpha i}\, {}^{\lambda}C_{\beta a} \quad , \qquad (1)$$

where $A_{i\to a}$ is the expansion coefficient and α and β are atomic orbitals.

A key quantity Ω (D,A) is determined by

$$\Omega(\mathrm{D},\mathrm{A}) = \sum_{\alpha\in\mathrm{D},\,\beta\in\mathrm{A}} \left(\mathrm{T}_{\alpha\beta}^{0\mathrm{i}}\right)^2 \tag{2}$$

The weights of local excitations on D and A are Ω(D,D) and Ω(A,A). The weight of electron transfer configurations D→A and A→D is represented by Ω(D,A) and Ω(A,D), respectively. The index Δq, which describes charge separation and charge transfer between D and A, is

$$\Delta\mathrm{q}(\mathrm{CS}) = \sum \Omega(\mathrm{D},\mathrm{A}) - \Omega(\mathrm{A},\mathrm{D}) \tag{3}$$

$$\Delta\mathrm{q}(\mathrm{CT}) = \sum \Omega(\mathrm{D},\mathrm{A}) + \Omega(\mathrm{A},\mathrm{D}) \tag{4}$$

In Tables 1 and 2, X = Ω(D,D) or Ω(A,A), and CT = Δq(CT).

Solvent Effects

The equilibrium solvation energy, $\mathrm{E}_\mathrm{S}^{\mathrm{eq}}$, of a molecule (in the ground or excited state) in the medium with the dielectric constant ε was estimated using a COSMO-like polarizable continuum model[41,42] in monopole approximation:

$$\mathrm{E}_\mathrm{S}^{\mathrm{eq}}(\mathrm{Q},\varepsilon) = -\frac{1}{2} f(\varepsilon)\mathrm{Q}^{+}\mathrm{D}\mathrm{Q} \tag{5}$$

where *f*(ε) is dielectric scaling factor, f(ε)=1-1/ε, **Q** is vector of *n* atomic charges in the molecular system, and **D** is *n* x *n* symmetric matrix determined by the shape of the boundary surface between solute and solvent. $\mathbf{D}=\mathbf{B}^{+}\mathbf{A}^{-1}\mathbf{B}$, where the *m* x *m* matrix **A** describes electrostatic interaction between *m* surface charges and the *m* x *n* **B** matrix describes the interaction of the surface charges with *n* atomic charges of the solute. The GEPOL93 scheme[43] was used to construct the molecular boundary surface.

The charge on atom X in the excited state Φ_i, $\mathrm{q}_\mathrm{X}^{\mathrm{i}}$, was calculated as:

$$\mathrm{q}_\mathrm{X}^{\mathrm{i}} = \mathrm{q}_\mathrm{X}^{0} + \Delta_\mathrm{X}^{\mathrm{i}}, \quad \Delta_\mathrm{X}^{\mathrm{i}} = \frac{1}{2}\sum_{\mathrm{Y}\neq\mathrm{X}}\sum_{\alpha\in\mathrm{X},\,\beta\in\mathrm{Y}} (\mathrm{T}_{\alpha\beta}^{0\mathrm{i}}\mathrm{T}_{\alpha\beta}^{0\mathrm{i}} - \mathrm{T}_{\beta\alpha}^{0\mathrm{i}}\mathrm{T}_{\beta\alpha}^{0\mathrm{i}}), \tag{6}$$

where $\mathrm{q}_\mathrm{X}^{0}$ is the atomic charge on X in the ground state and $\Delta_\mathrm{X}^{\mathrm{i}}$ is its change due to redistribution of the electron density caused by the excitation $\psi_0 \rightarrow \psi_\mathrm{i}$.

The non-equilibrium solvation energy for excited state ψ_i can be estimated as:

$$\mathrm{E}_\mathrm{S}^{\mathrm{neq}}(\mathrm{Q}^0,\Delta,\varepsilon,\mathrm{n}^2) = f(\varepsilon)\Delta^{+}\mathrm{D}\mathrm{Q}^0 - \frac{1}{2} f(\mathrm{n}^2)\Delta^{+}\mathrm{D}\Delta, \tag{7}$$

In Eq. (7), n^2 is optical dielectric constant of the medium and vector Δ describes the change of atomic charges in the molecule by excitation in terms of atomic charges, see Eq. (5).

Electron transfer rates

The rate of nonadiabatic ET, k_{ET}, can be expressed in terms of the electronic coupling squared, V^2, and the Franck-Condon Weighted Density of states (FCWD):

$$k_{ET} = \frac{2\pi}{\hbar} V^2 \, (FCWD) \tag{8}$$

that accounts for an overlap of vibrational states of donor and acceptor, and can be approximately estimated using the classical Marcus equation:

$$\left(FCWD\right) = \left(4\pi\lambda kT\right)^{-1/2} \exp\left[-\left(\Delta G^0 + \lambda\right)^2 \Big/ 4\lambda kT\right] \tag{9}$$

where λ is reorganization energy and ΔG^0 is standard Gibbs energy change of the process. The fragment charge difference (FCD)[44,45] method was employed to calculate the electronic couplings in this work.

The Marcus expression is derived for the high-temperature condition, $\hbar\omega_l \ll kT$, for all vibrational modes *l*. The semi-classical description of electron transfer (ET)[23,24] includes the effect of quantum vibrational modes in an effective way, the solvent (low frequency) modes are treated classically, while a single high-frequency intramolecular mode $\omega_i, \hbar\omega_i \gg kT$, is described quantum mechanically. Because ET occurs normally from the lowest vibrational level of the initial state, the rate *k* can be expressed as a sum over all channels connecting the initial state with the vibrational quantum number n = 0 to manifold vibrational levels of the final state,

$$k = \sum_{n=0}^{\infty} k_{0\to n} \text{ , where } k_{0\to n} = \frac{2\pi}{\hbar} V_{0\to n}^2 \frac{1}{\sqrt{4\pi\lambda_s kT}} \exp\left[-\frac{\left(\Delta G + \nu\hbar\omega_i + \lambda_s\right)^2}{4\lambda_s kT}\right] \text{,with}$$

$$V_{0\to n}^2 = V^2 \frac{S^n}{n!} \exp\left(-S\right) \tag{10}$$

An effective value of the Huang-Rhys factor *S* is estimated from the internal reorganization energy λ_i, $S = \lambda_i / \hbar\omega_i$

For organic systems, including fullerene derivatives, the main contribution to the internal reorganization energy is due to stretching of C=C bonds. Thus, the effective frequency was set to 1600 cm^{-1}.

Reorganization energy

The reorganization energy is usually divided into two parts, $\lambda = \lambda_i + \lambda_s$, including the internal and solvent terms. The solvent reorganization energy corresponds to the energy required to move solvent molecules from the position they occupy in the ground state to the location they have in the CT state, but without charge transfer having occurred. The λ_s for particular CT states were computed as a difference between equilibrium and non-equilibrium solvation energies. The internal reorganization energy λ_i corresponds to the energy of structural changes when the molecule goes from the initial-state geometry to the final-state geometry. The internal reorganization energy was estimated using the energy differences of the anion- and the cation- radicals taken in their equilibrium geometries as well as at geometries of the neutral species.

Conflicts of interest

There are no conflicts to declare.

Acknowledgements

We are grateful for financial support from the Spanish MINECO (Network RED2018-102815-T, project CTQ2017-85341-P, and Juan de la Cierva contract IJC2019-039846-I to A.J.S. and FJCI-2017-32757 to O.A.S.) and the Catalan DIUE (2017SGR39).

References:

1. F. C. Krebs, P. S. Larsen, J. Larsen, C. S. Jacobsen, C. Boutton and N. Thorup, *J. Am. Chem. Soc.*, 1997, **119**, 1208-1216.
2. A. Faldt, F. C. Krebs and N. Thorup, *J. Chem. Soc., Perkin Trans. 2*, 1997, 2219-2227.
3. N. Pavliček, A. Mistry, Z. Majzik, N. Moll, G. Meyer, D. J. Fox and L. Gross, *Nat. Nanotechnol.*, 2017, **12**, 308–311.
4. G. K. H. Madsen, F. C. Krebs, B. Lebech and F. K. Larsen, *Chem. - Eur. J.*, 2000, **6**, 1797-1804.
5. A. Heskia, T. Maris and J. D. Wuest, *Cryst. Growth Des.*, 2019, **19**, 5390-5406.
6. M. Yamamura, D. Hongo and T. Nabeshima, *Chem. Sci.*, 2015, **6**, 6373-6378.
7. M. Yamamura, T. Saito and T. Nabeshima, *J. Am. Chem. Soc.*, 2014, **136**, 14299-14306.
8. M. Yamamura, K. Sukegawa and T. Nabeshima, *Chem. Commun.*, 2015, **51**, 12080-12083.
9. M. Yamamura and T. Nabeshima, *Bull. Chem. Soc. Jpn.*, 2016, **89**, 42-49.
10. M. Yamamura, T. Hasegawa and T. Nabeshima, *Org. Lett.*, 2016, **18**, 816-819.
11. A. Heskia, T. Maris and J. D. Wuest, *Cryst. Growth Des.*, 2020, **20**, 1319-1327.
12. A. Heskia, T. Maris and J. D. Wuest, *Cryst. Growth Des.*, 2019, **19**, 5418-5428.
13. A. Heskia, T. Maris, P. M. Aguiar and J. D. Wuest, *J. Am. Chem. Soc.*, 2019, **141**, 18740-18753.
14. A. Heskia, T. Maris and J. D. Wuest, *Acc. Chem. Res.*, 2020, **53**, 2472-2482.
15. T. A. Schaub, K. Padberg and M. Kivala, *Chem. Lett.*, 2019, **48**, 1358-1367.
16. K. Morokuma, *J. Chem. Phys.,* 1971, **55**, 1236-1244.
17. T. Yanai, D. P. Tew and N. C. Handy, *Chem. Phys. Lett.*, 2004, **393**, 51-57.
18. F. Weigend and R. Ahlrichs, *Phys. Chem. Chem. Phys.*, 2005, **7**, 3297-3305.
19. D. Rehm and A. Weller, *Isr. J. Chem.* 1970, **8**, 259-271.
20. A. J. Stasyuk, O. A. Stasyuk, M. Solà and A. A. Voityuk, *J. Phys. Chem. B*, 2020, **124**, 9095-9102.
21. A. J. Stasyuk, O. A. Stasyuk, M. Solà and A. A. Voityuk, *Phys. Chem. Chem. Phys.,* 2019, **21**, 25098-25107.
22. A. J. Stasyuk, O. A. Stasyuk, M. Solà and A. A. Voityuk, *Chem. Commun.*, 2020, **56**, 12624-12627.
23. J. Jortner, *J. Chem. Phys.*, 1976**, 64**, 4860-4867.
24. J. Ulstrup and J. Jortner, *J. Chem. Phys.,* 1975, **63**, 4358-4368.
25. B. Küçüköz, B. Adinarayana, A. Osuka and B. Albinsson, *Phys. Chem. Chem. Phys.*, 2019, **21**, 16477-16485.
26. A. J. Stasyuk, O. A. Stasyuk, M. Solà and A. A. Voityuk, *J. Mater. Chem. C*, 2021, **9**, 9436-9445.
27. F. Neese, *WIREs Comput. Mol. Sci.*, 2012, **2**, 73-78.
28. F. Neese, *WIREs Comput. Mol. Sci.*, 2018, **8**, e1327.
29. S. Hirata and M. Head-Gordon, *Chem. Phys. Lett.*, 1999, **314**, 291-299.
30. S. Grimme, J. Antony, S. Ehrlich and H. Krieg, J. Chem. *Phys*., 2010, **132**, 154104.
31. S. Grimme, S. Ehrlich and L. Goerigk, *J. Comput. Chem.*, 2011, **32**, 1456-1465.

32. M. J. Frisch, G. W. Trucks, H. B. Schlegel, G. E. Scuseria, M. A. Robb, J. R. Cheeseman, G. Scalmani, V. Barone, G. A. Petersson, H. Nakatsuji, X. Li, M. Caricato, A. V. Marenich, J. Bloino, B. G. Janesko, R. Gomperts, B. Mennucci, H. P. Hratchian, J. V. Ortiz, A. F. Izmaylov, J. L. Sonnenberg, D. Williams-Young, F. Ding, F. Lipparini, F. Egidi, J. Goings, B. Peng, A. Petrone, T. Henderson, D. Ranasinghe, V. G. Zakrzewski, J. Gao, N. Rega, G. Zheng, W. Liang, M. Hada, M. Ehara, K. Toyota, R. Fukuda, J. Hasegawa, M. Ishida, T. Nakajima, Y. Honda, O. Kitao, H. Nakai, T. Vreven, K. Throssell, J. A. Montgomery, Jr., J. E. Peralta, F. Ogliaro, M. J. Bearpark, J. J. Heyd, E. N. Brothers, K. N. Kudin, V. N. Staroverov, T. A. Keith, R. Kobayashi, J. Normand, K. Raghavachari, A. P. Rendell, J. C. Burant, S. S. Iyengar, J. Tomasi, M. Cossi, J. M. Millam, M. Klene, C. Adamo, R. Cammi, J. W. Ochterski, R. L. Martin, K. Morokuma, O. Farkas, J. B. Foresman and D. J. Fox, GAUSSIAN 16 (revision A.03), Gaussian, Inc., Wallingford CT, 2016.
33. R. F. W. Bader, *Chem. Rev.*, **1991**, 91, 893– 928.
34. R. F. W. Bader, *Atoms in Molecules: A Quantum Theory*, Oxford University Press: Oxford, U.K., 1990.
35. E. Johnson, S. Keinan, P. Mori-Sánchez, J. Contreras-García, A. Cohen and W. Yang, *J. Am. Chem. Soc.*, 2010, **132**, 6498–6506.
36. J. Contreras-García, E. Johnson, S. Keinan, R. Chaudret, J. Piquemal, D. Beratan and W. Yang, *J. Chem. Theory Comput.*, 2011, **7**, 625–632.
37. G. A. Zhurko, Chemcraft 1.80 (build 523b) - graphical program for visualization of quantum chemistry computations. (https://chemcraftprog.com).
38. F. Plasser and H. Lischka, *J. Chem. Theory Comput.*, 2012, **8**, 2777-2789.
39. F. Plasser, S. A. Bäppler, M. Wormit and A. Dreuw, *J. Chem. Phys.*, 2014, **141**, 024107.
40. A. V.Luzanov and O.A. Zhikol, *Int. J. Quantum Chem.*, 2010, **110**, 902-924.
41. A. A. Voityuk and S. F. Vyboishchikov, *Phys. Chem. Chem. Phys.*, 2019, **21**, 18706-18713.
42. S. F. Vyboishchikov and A. A. Voityuk, *Phys. Chem. Chem. Phys.*, 2020, **22**, 14591-14598.
43. J. L. Pascual-Ahuir, E. Silla, and I. Tuñón, *J. Comp. Chem.*, 1994, **15**, 1127–1138.
44. A. A. Voityuk and N. Rösch, *J. Chem. Phys.*, 2002, **117**, 5607-5616.
45. A. A. Voityuk, *Phys. Chem. Chem. Phys.*, 2012, **14**, 13789-13793.